1 # RBL1 (p107) functions as tumor suppressor in glioblastoma

2 # and small-cell pancreatic neuroendocrine carcinoma

3 Thomas Naert[1,2,&], Dionysia Dimitrakopoulou[1,2,&], Dieter Tulkens[1,2], Suzan Demuynck[1], Rivka

4 Noelanders[1,2], Liza Eeckhout[1], Gert van Isterdael[3], Dieter Deforce[4], Christian Vanhove[2,5], Jo Van

5 Dorpe[2,6], David Creytens[2,6], Kris Vleminckx[1,2,7,§].

6 **[1]** Department of Biomedical Molecular Biology, Ghent University, Ghent, Belgium

7 [2] Cancer Research Institute Ghent, Ghent, Belgium

8 **[3]** Inflammation Research Center, VIB, Ghent, Belgium

9 [4] Laboratory for Pharmaceutical Biotechnology, Ghent University, B-9000 Ghent, Belgium

10 [5] Infinity lab, Ghent University Hospital, Ghent, Belgium

11 [6] Department of Pathology, Ghent University and Ghent University Hospital, Ghent, Belgium

12 [7] Center for Medical Genetics, Ghent University, Ghent, Belgium

13 [&] Contributed equally to this work

14 **[§] Corresponding author**

15 Kris Vleminckx, Ph.D.
16 Dept. for Biomedical Molecular Biology
17 Ghent University
18 Technologiepark 927
19 B-9052 Ghent (Zwijnaarde)
20 Tel +32-9-33-13760, Fax +32-9-221 76 73,
21 E-mail : kris.vleminckx@irc.UGent.be
22

23 **Competing interests**

24 The authors declare no competing interests.

25

26

Abstract

Alterations of the retinoblastoma and/or the p53 signaling network are associated with specific cancers such as high-grade astrocytoma/glioblastoma, small cell lung cancer (SCLC), choroid plexus tumors and small-cell pancreatic neuroendocrine carcinoma (SC-PaNEC). However, the intricate functional compensation between RB1 and the related pocket proteins RBL1/p107 and RBL2/p130 in suppressing tumorigenesis remains poorly understood. Here we performed lineage-restricted parallel inactivation of *rb1* and *rbl1* by multiplex CRISPR/Cas9 genome editing in the true diploid *Xenopus tropicalis* to gain insight into these *in vivo* compensatory mechanisms. We show that while *rb1* inactivation is sufficient to induce choroid plexus papilloma, combined *rb1* and *rbl1* inactivation is required and sufficient to drive SC-PaNEC, retinoblastoma and astrocytoma. Further, using a novel Li-Fraumeni syndrome-mimicking *tp53* mutant *X. tropicalis* line, we demonstrate increased malignancy of retinoblastoma-mutant neural malignancies upon concomitant inactivation of *tp53*. Interestingly, although clinical SC-PaNEC samples are characterized by abnormal p53 expression or localization, in the current experimental models, the *tp53* status had little effect on the establishment and growth of SC-PaNEC, but may rather be essential for maintaining chromosomal stability. SCLC was only rarely observed in our experimental set-up, indicating requirement of additional or alternative oncogenic insults. In conclusion, we used CRISPR/Cas9 to delineate the tumor suppressor properties of Rbl1 and generate new insights in functional compensation within the retinoblastoma protein family in suppressing pancreatic and specific neural cancers.

Keywords

Introduction

The interplay of the signaling networks controlling cell cycle (*e.g.* Retinoblastoma (RB)) and cell death (*e.g.* p53) in suppressing the development of cancers including, amongst others, glioblastoma, choroid plexus carcinoma, pancreatic neuroendocrine carcinoma and small-cell lung cancer was previously demonstrated by clinical and animal modeling studies [1–6]. Unsatisfactory, the median survival prospects for patients diagnosed with p53 and RB1 deficient cancers are extremely dismal, *e.g.* for small cell lung cancer (SCLC) (stage IV: 8-10 months [7]), small cell pancreatic neuroendocrine carcinoma (SC-PaNEC) (11 months [8]), choroid plexus tumors ($tp53^{mutated}$ WHO grade III: 2-4 months [9]) and glioblastoma (12-18 months [10]). As such, continued generation of novel and short latency preclinical models for these highly aggressive cancers remains necessary to fuel rational design of molecular targeted drug therapies.

Intriguingly, the RB signaling network entails a family of three pocket proteins (RB1, RBL1, RBL2), which in union tightly regulate G1/S cell cycle progression, and whose differential expression may underlie cell-type specific functional compensation in suppressing tumorigenesis [11,12]. An example of this compensation occurs in the mouse and *Xenopus* retina where RB1-deficiency fails to initiate retinoblastoma, and simultaneous inactivation of *Rbl1 (p107)* is required to initiate tumorigenesis [13–15]. In an alternative case, high-grade astrocytoma and choroid plexus tumors have been previously induced in murine models by overexpression of T_{121}, a truncated SV40 T antigen mutant that binds and inhibits RB1, RBL1 and RBL2 proteins [16,17]. In order to investigate the selective tumor suppressor properties of the Rbl1 protein, thus dissecting compensation on a genetic level, we performed concomitant inactivation of the *rb1* and *rbl1* tumor suppressor genes, leaving *rbl2* unaltered. For this we used CRISPR/Cas9 gRNA ribonucleoproteins (RNPs) delivered by microinjection in embryos of *Xenopus tropicalis*, an aquatic amphibian with an unique true diploid genome. By targeting the injections to specific blastomeres we were able to modify the retinoblastoma signaling network in different tissue lineages, including the neural and pancreatic lineages [18,19]. As such, we aimed to obtain a deeper understanding of tissue-specific compensation between RB1 and RBL1 in cancer development [20].

Next to manipulating the RB pathway, we also generated a *tp53* knockout *Xenopus* line as a stable genetic background with a twofold aim. We wanted to explore whether Li-Fraumeni syndrome (LFS) could be recapitulated in *Xenopus tropicalis*. In addition, we wanted to investigate whether *tp53* deficiency sensitizes the animals to tumor initiation or progression upon additional genetic oncogenic insults, as has been extensively documented in the mouse. LFS is a cancer syndrome defined by either incapacitating germline *TP53* mutations or *de novo* mutations occurring during early embryogenesis [21,22]. LFS patients are at risk for development of (osteo-)sarcomas, central nervous system (CNS) tumors,

3

82   breast cancer and adrenocortical carcinoma, as well as other less frequent cancers [23]. Previously, *Tp53*

83   knockout mouse models have been generated and were shown to be prone to the development of a

84   variety of cancers, most frequently lymphomas and sarcomas [24–26]. Additionally, LFS was modeled in *tp53*

85   mutant zebrafish spontaneously developing malignant peripheral nerve sheet tumors (MPNST) and

86   angiosarcoma, next to other tumor types [27,28].

87   As mentioned before, p53 is an established gatekeeper for numerous tumor types. Hence,

88   experimental oncogenic insults, either genetic or environmental, are frequently employed in a *Tp53*

89   mutant background because it increases tumor penetrance and reduces tumor latency. As such, we also

90   performed parallel perturbation of the retinoblastoma and p53 signaling network, by multiplexing *rb1,*

91   *rbl1* CRISPR/Cas9 and inactivating *tp53* by either CRISPR/Cas9 multiplexing or breeding efforts. We

92   investigated whether sensitizing *Xenopus tropicalis* to cancer development by perturbing p53 functions

93   could alter the tumor spectrum occurring upon perturbations in the retinoblastoma signaling network. In

94   this regard, previous work also described that concomitant perturbation of the retinoblastoma and p53

95   signaling network generates chromosomal instability (CIN), possibly sensitizing to cancer development [29–

96   31].

97   By our *in vivo* gene editing strategy we identify novel cell-type specific requirements for inactivation

98   of *rbl1,* in order to bypass compensation in the native and immunocompetent *Xenopus* brain and

99   pancreas upon inactivation of *rb1*, across different *tp53* genotypes. By combinatorial CRISPR/Cas9

100 editing of *rb1* and *rbl1* we demonstrate highly penetrant development of SC-PaNEC, glioblastoma,

101 choroid plexus tumors, next to other cancer types. Interestingly, we provide genetic evidence

102 establishing *rbl1* as a genuine tumor suppressor in SC-PaNEC and glioblastoma.

103 We believe our novel genetic *X. tropicalis* genetic cancer models have the potential to generate

104 important molecular insights and could emerge as promising preclinical cancer models [32]. Namely, these

105 *Xenopus* cancer models are uniquely positioned as an alternative to viral vector-mediated CRISPR/Cas9

106 mice models, mainly due to the relative ease of CRISPR/Cas9 delivery and the short latency and high

107 penetrance of cancer development [33] .

108 **Results**

109 ***tp53* mutant *X. tropicalis* develop hematological malignancy and sarcomas reminiscent of Li-Fraumeni**

110 **syndrome**

4

111   In order to generate a *tp53* mutant *X. tropicalis* line, we unilaterally injected *tp53* coding region 1

112   (*tp53*[cr1]) gRNA precomplexed with recombinant Cas9 protein in two-cell *X. tropicalis* embryos. Mosaic

113   mutant F0 animals, further called crispants, were raised until sexual maturity and out-crossed with wild-

114   type animals. Upon targeted amplicon sequencing and BATCH-GE analysis [34], we selected two types of F1

115   *tp53* heterozygotes, each with a distinct variant of a Δ4 deletion (*tp53*$^{\Delta4var1/+}$ and *tp53*$^{\Delta4var2/+}$) (Table S1A).

116   Both of these deletions are expected to give rise to nonsense-mediated decay since due to the frame-

117   shifting deletion, the pre-mRNA contains a premature stop codon (*tp53*^{168STOP}). These heterozygote

118   mutants (F1) were subsequently intercrossed (*tp53*$^{\Delta4var1/+}$ x tp53$^{\Delta4var2/+}$) to obtain F2 homozygous mutant

119   animals (*tp53*$^{\Delta4var1/\Delta4var2}$) (Table S1B). Both the hetero- and homozygous mutant animals were monitored

120   for morbidity and euthanized at ethical endpoint defined by distended abdomen reminiscent of ascites,

121   lethargy, or decreasing body weight. Of note, *X. tropicalis* has a significantly longer lifespan than murine

122   animal models and can reach over ten years of age in experimental housing conditions.

123   Kaplan-Meier analysis over a period of 900 days revealed faster occurrence of morbidity in two

124   clutches of *tp53*$^{\Delta4var1/\Delta4var2}$ (F2) nullizygous animals when compared to *tp53* heterozygotes (F1) ($p < 0.01$;

125   Table S2A) (Fig. 1A). We investigated moribund mutant *X. tropicalis* by X-ray techniques, revealing

126   calcified ectopic structures in 66% (n=3) of F1 *tp53* heterozygous animals (Fig. 1B).

127   In order to investigate the possible presence of hematological malignancy, we performed

128   immunohistological analysis of the spleen in moribund *tp53* mutant animals. In the wild type *Xenopus*

129   spleen, CD3^{+} cells organize in a ring-like structure surrounding the white pulp, which contains the B-cells

130   and displays pronounced PCNA immunoreactivity (Fig. 1C-left) [35]. However, this CD3^{+} ring-like structure

131   was disrupted in 75% (n=8) of the moribund *tp53*$^{\Delta4var1/\Delta4var2}$ animals (Fig. 1C-right; Fig. 1D). In 25% (n=8)

132   of these animals we also observed that PCNA immunoreactivity expanded into red pulp areas not

133   contiguous with CD3 immunoreactivity. As such, we conclude that the observed splenic architectural

134   disruptions are reflecting the presence of different hematologic malignancies either or not of the T-cell

135   lineage, which in one case lead to profound cleaved caspase-3 immunostaining in splenic white pulp (Fig.

136   S1A). Interestingly, both malignancies of the B- and T-cell lineages have been described in murine *tp53*

137   mutant animals models [36].

138   In order to further investigate the presence of T-cell-related hematological malignancy in

139   *tp53*$^{\Delta4var1/\Delta4var2}$ animals, peripheral blood of remaining non-moribund littermates (n=6) was collected by

140   toe clipping and subjected to flow cytometry to investigate the proportion of cells of the T-cell lineage.

141   Enrichment of CD3^{+} (cytoplasmic or membrane located) and CD8^{+} cells could be demonstrated in one out

142   of six of the non-moribund animals (Fig. 1F; Fig. S2-3). An increased leukocyte count was subsequently

143   validated by Natt-Herrick's method in blood obtained by cardiac bleed in this animal, when compared to

144   an age-matched control ($p < 0.01$; Table S2B) (Fig. 1E; Fig. S1B). Furthermore, in this $tp53^{-/-}$ animal, $CD3^+$

145   cells were also disorganized in the spleen and diffuse dissemination of $CD3^+$ T-lymphocytes could be

146   observed in the liver (Fig. 1G; Fig. S1C). Furthermore, we also observed the presence of liposarcoma in

147   one $tp53^{-/-}$ animal (Fig. S1D).

148   Finally, one moribund *tp53* heterozygous animal presented with a large intraperitoneal lobular

149   neoplasm, classified by histopathology as a high-grade undifferentiated spindled and round cell sarcoma

150   with profound PCNA proliferation marker immunoreactivity (Fig. 1H).

151   Taken together, we demonstrate development of a LFS-type tumor spectrum with hematological

152   malignancy and sarcoma in *tp53* mutant *X. tropicalis*, in line with well-characterized *Tp53* mutant mouse

153   models [24,25]. The latency to neoplasm-related morbidity (> 1 year) is relatively long in the *tp53* mutant *X.*

154   *tropicalis*, but can likely be attributed to the relative long lifespan (~ 10 years) of *Xenopus*. In any case,

155   these animals constitute a valuable platform for evaluating the role of the *tp53* tumor suppressor gene

156   inactivation in combination with other oncogenic insults. Hence, we continued on to target

157   retinoblastoma-family tumor suppressor genes in this *tp53* mutant line.

Induction of small-cell pancreatic neuroendocrine carcinoma (SC-PaNEC) by CRISPR/Cas9 genome

159   **editing**

160   In order to investigate the functional consequences of inactivating *rb1* and *rbl1*, under differential

161   *tp53* genetic backgrounds, we performed multiplex CRISPR/Cas9-mediated inactivation of these genes in

162   *tp53* mutant and wild-type *X. tropicalis*. Note that the *rb1* and *rbl1* gRNAs used throughout this study

163   have previously been reported to induce retinoblastoma in *X. tropicalis* [14]. These gRNAs were shown to

164   induce retinoblastoma independent from CRISPR/Cas9 off-target effects, as in that study another pair of

165   *rb1/rbl1* gRNAs with a differential genomic targeting site similarly induced this tumor type. For targeting

166   *tp53*, we also included a gRNA that was different from the one used to make the KO line, *i.e. $tp53^{coding}$*

167   *$^{region\ 2}$ or $tp53^{cr2}$.*

168   We intercrossed $tp53^{\Delta4var1/+}$ with $tp53^{\Delta4var2/+}$, generating embryos with either $tp53^{+/+}$, $tp53^{\Delta4var1/+}$,

169    $tp53^{\Delta4var2/+}$ or $tp53^{\Delta4var1/\Delta4var2}$ genotype, while simultaneously intercrossing wild-type (WT) *X. tropicalis* to

170   obtain WT embryos. We subsequently injected *tp53* mutant or WT embryos in the eight-cell stage in a

171   single vegetal-dorsal blastomere with distinct combinations of tumor suppressor-targeting CRISPR/Cas9

172   RNPs (Fig. 2A). As thus we performed primarily genome editing of the anterior endoderm, including the

173   pancreas. Genome editing was confirmed by targeted amplicon sequencing and BATCH-GE analysis

6

174   (Table S1C). Animals were euthanized when presenting with distended abdomen, lethargy and

175   decreasing bodyweight or at end-of-experiment (97 days). Necropsy revealed no gross pancreatic

176   abnormalities in animals resulting from *rb1* CRISPR/Cas9 injection in embryos obtained from a *tp53*$^{Δ4var1/+}$

177   x *tp53*$^{Δ4var2/+}$ intercross (hereafter termed single mosaic knockout (**smKO**) at 97 days (n=13). However, we

178   observed pancreatic dysmorphology in 86% (n=29) of the animals resulting from multiplexed *rb1/rbl1*

179   CRISPR/Cas9 injection in embryos obtained from the same intercross (hereafter termed double mosaic

180   knockout (**dmKO**)) and in 77% (n=22) of the animals resulting from *rb1/rbl1/tp53*^{cr2} CRISPR/Cas9 injection

181   in WT embryos (hereafter termed triple mosaic knockout (**tmKO**)). Both for dmKO and tmKO, these

182   pancreatic dysmorphologies were observed prior to the 70 day timepoint (Fig. 2B-C; Table S2C).

183   Histologically, we observed cellular, poorly differentiated malignant tumors with a 'small blue round cell'

184   morphology, cellular pleomorphism, high mitotic activity and foci of hemorrhage and necrosis,

185   compatible with the histology of SC-PaNEC (Fig. 2D) [37]. A high proliferative index was demonstrated

186   further by both anti-proliferating cell nuclear antigen (PCNA) and anti-Ser10 phosphorylated histone H3

187   (pHH3) immunostaining (Fig. 2E).

188   ***Tp53* mutations are not essential for small-cell pancreatic neuroendocrine carcinoma (SC-PaNEC)**

189   **formation**

190   The near-complete penetrance of SC-PaNEC development in dmKO animals, which are derived from a

191   *tp53*$^{+/-}$ intercross wherein 75% of the individuals are expected to have at least one wild-type copy of

192   *tp53,* provided preliminary evidence that *tp53* does not have an essential gatekeeper function in

193   preventing SC-PaNEC tumorigenesis. In order to validate this further, we first performed genotyping of

194   *tp53* in each dmKO animal and showed that indeed the clutch followed expected Mendelian ratios (H_0 =

195   non-Mendelian; p = 0.63) (Table S1D and S2D) [38]. We observed no correlation between *tp53* genotype

196   and incidence of SC-PaNEC development (p > 0.05; Table S2E) or between SC-PaNEC size and *tp53*

197   genotype (p > 0.05; Fig. S4A; Table S2E). Furthermore, no obvious differences in cell death between *tp53*$^{-}$

198    $^{/-}$ or *tp53*$^{+/+}$ SC-PaNECs could be demonstrated by TUNEL staining (Fig. S4B). In fact, SC-PaNEC cells do not

199   show TUNEL positivity, in stark contrast to the immediately surrounding normal pancreatic cells, possible

200   due to cellular stress from the adjacent neoplasm. Finally, investigation of SC-PaNEC proliferation

201   characteristics across different *tp53* genotypes, by quantification of pHH3 positive cells in tissue sections,

202   did not reveal any genotype-specific differences (Fig. S4C; Table S2F).

203   Interestingly, the genetic make-up of the *tp53* nullizygous mutant animals, with a distinct Δ4 variant

204   on each chromosome, allows assessment of genomic instability on chr3.p. For this, we performed laser

205   capture microdissection (LCM) and *tp53* genotyping of SC-PaNECs from the dmKO. We observed

206   chromosomal instability (aneuploidy) involving chr3.p in 66% (n=3) of $tp53^{-/-}$ SC-PaNECs in the dmKO

207   setup (Fig. 2F; Table S1E; Fig. S5). In contrast, $tp53^{+/-}$ SC-PaNEC (n=3) in the dmKO retained the expected

208   allelic ratios, demonstrating that *tp53* LOH is not occurring and that SC-PaNECs can initiate without bi-

209   allelic germline mutations in *tp53* (Fig. 2F; Fig. 2G - blue ovals). Confirming this further, we showed by

210   similar LCM and genotyping methodology that two tumors in the tmKO setup (n=7) developed without

211   biallelic CRISPR/Cas9-mediated inactivation of the *tp53* gene (red ovals – Fig. 2G) . Taken together, we

212   found that inactivation of *tp53* is not essential for SC-PaNEC tumor initiation, but provide, albeit

213   preliminary, evidence that its inactivation might drive genomic instability [31].

214   ***Rbl1* functions as a tumor suppressor in SC-PaNEC**

215   Given that we could not detect any development of SC-PaNECs in smKO (*rb1* mosaic mutant) animals,

216   but SC-PaNECs were readily detected in *rb1/rbl1* double mosaic mutants (dmKO and tmKO animals), we

217   hypothesized that *rbl1* is functioning as a genuine tumor suppressor gene in SC-PaNEC.

218   Previously, multiplex CRISPR/Cas9 technology has been described as a platform enabling *in vivo*

219   functional interrogation of genes in pancreatic ductal carcinoma [39,40]. Namely, genes functioning as

220   genuine tumor suppressors are found to be mutated in tumors due to positive selection for inactivating

221   genomic alterations. We had also previously demonstrated similar positive selection pressure on

222   combined *rb1* and *rbl1* inactivation in a pediatric *X. tropicalis* retinoblastoma model [14].

223   We performed LCM of SC-PaNECs, followed by both *rb1* and *rbl1* genotyping. We could demonstrate

224   fully penetrant positive selection pressure for both *rb1* and *rbl1* mutations in SC-PaNECs from tmKO

225   (100%; n=7) animals (Table S1F). Similarly, positive selection for simultaneous *rb1* and *rbl1* mutations

226   was found in SC-PaNECs from dmKO (100%; n=6) animals (Fig. 2G). Overall, our data shows that *rb1*

227   inactivation alone, irrespective of *tp53* genotype, is not sufficient to initiate SC-PaNEC in *X. tropicalis.*

228   This appears to be due to redundancy with the *rbl1* gene, since we demonstrate that inactivation of the

229   retinoblastoma pathway by multiplex *rb1/rbl1* inactivation results in highly penetrant SC-PaNEC

230   formation with short latency.

231   **Highly penetrant induction of central nervous system tumors in *rb1* and *rbl1* double mosaic mutants**

232   Given the non-necessity for *tp53* inactivation in SC-PaNEC development, we further aimed to provide

233   a proof-of-principle that p53 can indeed have tumor suppressive functions in other *X. tropicalis* Rb1-

234   deficient cancers. We performed ectoderm-specific CRISPR/Cas9-mediated genome editing of *rb1* and

8

235   *rbl1* in embryos obtained from a tp53$^{\Delta4var1/+}$ and tp53$^{\Delta4var2/+}$ intercross, via injection of an animal-dorsal

236   blastomere (Fig. 3A) (Table S1G). Animals were euthanized at metamorphic climax (69 days post-

237   injection) and necropsy revealed that 75% (n=16) of the animals presented with externally visible

238   retinoblastoma development (Fig. 3B). Furthermore, 44% (n=16) of the animals had excessive black skin

239   pigmentation, indicative of a disturbed neuroendocrine reflex in the pituitary or hypothalamus for the

240   regulation of pigment dispersion in dermal melanophores (Fig. 3B-C) [41]. This prompted us to investigate

241   the animals for CNS abnormalities. Genotyping of *tp53* was performed by targeted amplicon sequencing

242   for each animal within the setup (Table S1H). Histopathology revealed presence of retinoblastoma and

243   brain-located poorly differentiated and highly malignant small blue round cell tumors (SBRCTs), in

244   respectively 75% and 43% (n=16) of the animals, closely recapitulating previously reported

245   retinoblastoma incidences in *rb1/rbl1* crispants (Fig. 3D) [14]. The SBRCTs (Fig. 3E – white arrows) likely

246   correspond to either invasive retinoblastoma, pinealoblastoma (trilateral retinoblastoma) or possibly

247   medulloblastoma [42]. In any case, SBRCTs presented with aggressive growth characteristics as indicated by

248   PCNA immunoreactivity (Fig. S6A). Comparison of retinoblastoma and SBRCTs incidences across *tp53*

249   genotype did not reveal any clear correlation ($p > 0.05$; Table S2G). Furthermore, in line with previously

250   published studies in the mouse, histopathological hallmarks of *rb1/rbl1* inactivated retinoblastoma did

251   not change upon *tp53* pathway inactivation [43]. Interestingly however, we also observed penetrant

252   induction of choroid plexus neoplasms (Fig. 3E – black arrow) and glioblastoma (Fig. 3E – red arrow) in

253   the CNS of *tp53*$^{\Delta4var1/\Delta4var2}$ animals (Fig. S6B). Therefore, we first performed a differential analysis

254   comparing the grade and incidence of choroid plexus tumors across *tp53* genotypes.

255   ***Tp53* mutational status underlies retinoblastoma-mutant choroid plexus tumor progression**

256   Having observed the presence of choroid plexus tumors (CPT) in *rb1* and *rbl1* double crispant tadpoles,

257   we aimed to investigate whether, in line with the clinical data, *tp53* inactivation is linked with an

258   increased CPT grade [9]. For this, anonymized sections from choroid plexi (n=15) were analyzed by a

259   pathologist and classified according to clinical WHO grading criteria in one of three categories: normal,

260   grade 1 (G1) (choroid plexus papilloma) or >G1 (atypical choroid plexus papilloma and choroid plexus

261   carcinoma) [44]. Normal amphibian choroid plexus closely resembles the mammalian structural

262   organization, where ependymal cells, capillaries and pia mater can be readily discriminated at high

263   magnification (Fig. 4A). G1 neoplasms were characterized by cellular disarray, (pseudo-)stratification and

264   loss of polarization (Fig. 4A –arrow), while mitotic figures were relatively rare. In higher grade (>G1)

265   neoplasms, pronounced cellular disarray and severely increased mitotic figures could be observed. Clear

266   continuity between normal choroid plexus (CP) and neoplasms was also demonstrated (Fig. 4B). By this

267   subclassification, a correlation between *tp53* genotype and choroid plexus neoplasm grade could be

268   demonstrated ($p < 0.01$; Table S2H) (Fig. 4C). Furthermore, immunofluorescence, in a $tp53^{\Delta4var1/\Delta4var2}$

269   animal, further revealed profound PCNA immunoreactivity in a >Grade 1 neoplasm, demonstrating high

270   proliferative activity (Fig. 4D – white arrow).

271   Finally, we performed LCM and targeted amplicon sequencing of the *tp53* locus in choroid plexus

272   tumors and control tissue (Fig S7; Table S1I). As described previously for PaNECs, the genetic make-up of

273   the *tp53* homozygous mutant animals allows assessment of genomic instability on chr3.p. In

274   $tp53^{\Delta4var1/\Delta4var2}$, the >G1 choroid plexus neoplasms exhibited either loss of compound heterozygosity or

275   hyperploidy of one Δ4-variant, while control tissue (normal brain, bone) exhibited the expected normal

276   allelic ratios (50% each variant) (Fig. 4E - left). Furthermore, in a high-grade CP lesion in a heterozygous

277   *tp53* mutant animal, we could demonstrate LOH of the remaining WT *tp53* allele (Fig. 4E – right). We

278   found lack of positive selection pressure for *rbl1* mutations, as we observed that the *rbl1* allele remained

279   wild-type in *tp53* nullizygous CPTs (n = 3) (Table S1J). As such, *rbl1* does not appear to function as a

280   tumor suppressor gene in CPTs.

Rbl1 functions as a tumor suppressor in glioma, while _tp53_ inactivation underlies malignant progression

283

284   Further analyzing the CNS of *rb1* and *rbl1* multiplex CRISPR/Cas9-engineered animals obtained from a

285   tp53$^{\Delta4var1/+}$ and tp53$^{\Delta4var2/+}$ intercross, we also observed the occurrence of glioma with pronounced

286   intratumoral heterogeneity in 81% (n=16) of these animals. A significant correlation between *tp53*

287   genotype and glioma grade was present, with high-grade glioblastoma lesions only seen in $tp53^{\Delta4var1/\Delta4var2}$

288   animals ($p < 0.001$) (Fig. 5A,B; Fig. S8A) (Table S2I). In line with murine *Rb1*-mutant glioblastoma, high-

289   grade lesions were characterized by the presence of pleomorphic giant cells, mitotic defects and massive

290   nuclear aneuploidy (Fig. 5A, B) (Supplemental Movie 1) [5,45]. In depth microscopic analysis of these

291   nuclear abnormalities showed some to be interconnected across distances spanning tens of micrometers

292   (Supplemental Movie 2). In the higher grade lesions, the giant cells were also interspersed with smaller

293   rounder cells with dense nuclei. Here, both cell-types possessed a high proliferative index as

294   demonstrated by PCNA immunostaining (Fig. 5E). Furthermore, we showed heterogeneous

295   immunoreactivity to a GFAP antibody throughout these actively cycling cells, in line with literature and

296   validating astrocytic origin (Fig. S8C) [10]. Glioblastoma cells were observed predominantly in areas

297   contiguous with normal proliferative areas (subventricular zone), especially in the forebrain (Fig. 5B-C),

298   but also in regions not immediately spatially associated with such proliferative zones. Areas of

299   pseudopallisading necrosis or hemorrhaging were absent. We found profound EZH2 immunoreactivity in

300   forebrain lesions associated with the SVZ, pointing to a proneural glioblastoma, at least at this

301   anatomical location (Fig. 5E; Fig. S8B) [46,47]. Unfortunately, further attempts to perform glioblastoma

302   subtyping were unsuccessful, due to lack of suitable antibodies in *Xenopus tropicalis.*

303   The presence of astrocytoma in animals exclusively mutant in *rb1* and *rbl1* (Fig. 5A, D), pruned us

304   to investigate whether *rbl1* compensates for the loss of *rb1*, under *tp53* wild-type conditions. For this, we

305   performed a retrospective analysis of brain sections from our previously published retinoblastoma study

306   in animals unilaterally targeted at the two-cell stage with *rb1* and *rbl1* gRNA [14]. We detected the

307   presence of astrocytoma in 100% (n=9) of the animals injected with the *rb1/rbl1* gRNAs (Fig. S9).

308   Astrocytoma was also found in animals injected with another pair of *rb1/rbl1* gRNA, ruling out potential

309   CRISPR/Cas9 off-target effects as contributing to the observed phenotype. Interestingly, some

310   astrocytoma lesions in this cohort had spontaneously progressed to high-grade glioblastoma,

311   demonstrating that *rb1/rbl1*-deficient glioma progression is indeed possible *in vivo* (Fig. S9 - black arrow).

312   We further wanted to investigate whether the requirement for *rbl1* inactivating mutations can

313   be overruled by additional oncogenic insults. Co-inactivation of *pten* was chosen as this gene has been

314   widely linked to glioblastoma malignancy [5,48]. Therefore, we performed ectoderm-specific CRISPR/Cas9-

315   mediated genome editing of *rb1* and *pten^{cr1}* in embryos obtained from a tp53$^{\Delta4var1/+}$ and tp53$^{\Delta4var1/+}$

316   intercross, thus leaving *rbl1* intact (Table S1K). Animals were euthanized at day 42 and histopathology

317   revealed absence of any glioma (0%; n=14) in either of the three *tp53* genotypes, including four

318   *tp53$^{\Delta4var1/\Delta4var1}$* animals (Fig. 5D, Table S1L). In contrast, animals injected with *rb1, rbl1, tp53^{cr2}* and *pten^{cr2}*

319   in the ectodermal lineage demonstrated complete penetrance in high-grade glioblastoma development

320   (100%; n=13) at day 42 (Fig. 5C-D; Table S1M).

321   Collectively, our experiments provide the direct genetic evidence that *rbl1* functions as a tumor

322   suppressor compensating for loss of rb1 in *rb1*-mutant astrocytes and that concomitant inactivation of

323   *rb1/rbl1* is sufficient for glioma initiation. Further, and in line with literature, we demonstrate that *tp53*

324   inactivation facilitates progression of retinoblastoma-deficient glioma to high-grade glioblastoma [5].

325

326   **Discussion**

327   Members of the retinoblastoma pocket protein family (RB1, RBL1, RBL2) play a pivotal role in the

328   control of cellular proliferation and their direct inactivation by mutational events has been previously

11

329   implicated in cancers, such as small-cell lung carcinoma (SCLC) and retinoblastoma [13,49]. However,

330   contemporary approaches for understanding and modeling cancer has conceptualized that signaling

331   networks can be disturbed at diverse nodes, converging on similar downstream phenotypical

332   consequences. For instance, within the RB signaling network, the ability of RB1 and RBL1 to regulate the

333   cell cycle can be bypassed by events altering their common upstream cyclin dependent kinase regulators

334   (*i.e* CDK4, CDKN2A/p16). Such direct genetic deregulation of the RB signaling network by either *CDK4*

335   amplification, or inactivation of *CDKN2A/B* or *RB1*, had been previously shown in human SC-PaNEC and

336   glioblastoma [4,50–52]. In contrast, direct genetic inactivation of *RBL1* (*p107*) remains rare (<0.5%) in clinical

337   glioma samples. However, reanalyzing cancer genomic data for combined cohort of 8 glioma studies

338   validated mutual exclusivity between *CDNK2A/B* and *CDK4* alterations ($p < 0.001$), but established

339   significant co-occurrence of *RB1* and *RBL1* alterations ($p = 0.034$) (Table S3) [53,54]. As such we postulate

340   that directly inactivating *rb1* and *rbl1* could contribute to cancer initiation, similar to indirect

341   simultaneous inactivation of RB1 and RBL1 protein function due to prolonged phosphorylation by

342   upstream Cyclin/CDK complexes. This hypothesis is further supported by reports that RBL1 is

343   downregulated in glioma tumors and cell lines [55]. Furthermore, *Rb1* deficiency alone fails to initiate

344   tumorigenesis in astrocytes, while transgenic *in vivo* expression of a truncated SV40 large T antigen (T_{121}),

345   which binds and inhibits all three retinoblastoma family members, is sufficient for tumorigenesis [56].

346   Additionally, a *Rb1/Rbl1/Tp53/Pten* conditional murine glioblastoma model was previously generated

347   and used as a platform for preclinical studies [47,57]. However because the full characterization of this line

348   is, up to this date, not reported we cannot delineate the exact impact of *Rbl1* inactivation. Finally, it was

349   shown that *Rbl1*-deficient mice exhibit expanded neural stem cell population and impaired commitment

350   of neuronal progenitors to a neuronal fate, showing previously underappreciated functions of Rbl1 [58,59].

351   In fact, to our knowledge the definitive genetic *in vivo* elucidation of *RBL1* as a glioma tumor suppressor

352   has not been reported before. Here we showed that *rbl1* inactivation is a cooperative event in the rapid

353   establishment of glioma in immunocompetent *rb1*-deficient *Xenopus tropicalis*. Furthermore, we believe

354   that while direct genetic inactivation of the *RBL1* gene is rare (0.3%) in glioma, additional mechanisms

355   are at play in which the RBL1 protein could in fact be a major player in suppressing tumorigenesis, but

356   has had its role previously seen minimized due to its indirect inactivation at a functional level.

357   We also demonstrate that concomitant inactivation of *rb1* and *rbl1* is sufficient to induce SC-PaNEC.

358   Unfortunately, as a consequence of the low incidence of SC-PaNEC, no large sets of whole-exome or

359   whole-genome sequencing data are available to address the status of the *RBL1* gene in clinical SC-PaNEC.

360   Nevertheless, previous studies already suggested functional compensation between pocket proteins in

361   the endocrine pancreas, where inactivation of *Rb1* has little effect on β-cell replication, while

362   concomitant *Rb1/Rbl1* and *Rb1/Rbl2* inactivation has profound impact on proliferation and apoptosis [60–

363   62].

364   In contrast to these newly discovered *rbl1* tumor suppressor roles, we also show that choroid plexus

365   tumorigenesis does not critically depend on *rbl1* inactivation. Additionally, while we had previously and

366   incidentally discovered a small cell lung carcinoma in a *rb1/rbl1* crispant [14], we fail to identify these in

367   larger cohorts of *rb1/rbl1* crispants, across different *tp53* genotypes. Interestingly, this is in line with

368   mice modeling data placing *Rbl2* (*p130*), and not *Rbl1,* at the center of tumor suppression in *rb1*-deficient

369   endocrine lung cells [49]. This reflects, cell-type specific responses to inactivation of distinct retinoblastoma

370   network elements, whose interplay could be further dissected using CRISPR/Cas9 in *Xenopus* [11].

371   Furthermore, we also co-interfered with the cell signaling death network by targeting *tp53*, in order

372   to gain insight in how co-occurring p53 aberrations influences *rb1/rbl1*-deficient cancers. In contrast to

373   the accepted paradigm that concomitant p53 and retinoblastoma signaling network abnormalities are

374   required to initiate SC-PaNEC, we demonstrate unexpected low impact of *tp53* inactivation in *rb1/rbl1*-

375   inactivated SC-PaNEC [2]. In line with our results, the implication of p53 in clinical SC-PaNEC is

376   predominated by abnormal immunostaining of the p53 protein, rather than absence of reactivity, which

377   would be indicative for p53 loss-of-expression [63,64]. We speculate that *TP53* mutational events could be

378   dispensable in early SC-PaNEC tumorigenesis, but that *TP53* alterations and their consequent

379   chromosomal instability could eventually leads to highly malignant and metastatic SC-PaNEC [29].

380   Unfortunately SC-PaNEC is considered to be unresectable and mostly metastatic at the time of diagnosis

381   and hence patients are almost immediately treated with chemotherapy, precluding clinical assessment

382   of *TP53* alterations in early stages of SC-PaNEC development. Regrettably, the tumors in our *Xenopus*

383   model are too fast growing, leading to morbidity and ethical endpoint prior to metastasis formation,

384   impeding assessment of this hypothesis.

385   In contrast to the above and closely recapitulating the known roles of p53, we demonstrate that in

386   CPTs and glioblastoma, wild-type *X. tropicalis* p53 is able to limit tumor progression. Namely, *tp53*

387   nullizygous choroid plexus tumors and gliomas demonstrate more malignant histological characteristics,

388   higher proliferation and increased chromosomal instability, in line with the published clinical human and

389   mice experimental data [3,9,65].

390   In this paper we also describe the first *tp53* nullizygous *X. tropicalis* line and demonstrate that

391   *Xenopus tp53* behaves, analogous to *TP53* in Li-Fraumeni, as a tumor suppressor gene for syndromic

392   *Xenopus* cancer development. We demonstrate that *tp53* mutations are predisposing for a Li-Fraumeni

13

393   tumor spectrum, namely hematological malignancies and sarcomas, admittingly with a long latency of >1

394   year. We believe the latter to be attributable to the life-span of *X. tropicalis* that is substantially longer

395   (>3x) than mice and may also underlie interspecies physiological differences. Interestingly, our

396   *tp53*$^{\Delta 4var1/\Delta 4var2}$ compound heterozygote line enables easy identification of each *tp53* allele. This allows

397   tracking of local chromosomal instability during cancer initiation and progression by straightforward

398   amplicon sequencing of both distinct *tp53* CRISPR/Cas9 deletion scars, permitting rapid assessment of

399   *tp53* focal amplification, aneuploidy events or loss of heterozygosity.

400   When comparing our novel *X. tropicalis* cancer models to established zebrafish models, neither *tp53*

401   nor *rb1* mutant zebrafish have been reported to develop Li-Fraumeni-related hematological

402   malignancies, SC-PaNEC or CPT [27]. In fact, in contrast to the clinical situation, *tp53* mutant fish develop

403   predominantly malignant peripheral nerve sheath tumors and *rb1* TALENs F0 edited *tp53* mutant fish

404   develop primitive neuro-ectodermal tumors and medulloblastoma [66,67].

405   In the comparison to established mammalian cancer models, we believe that *Xenopus* holds unique

406   experimental advantages such as extremely straightforward tissue-restrictive CRISPR/Cas9 delivery and

407   multiplexing in externally developing embryos [18]. Additionally, the *X. tropicalis* SC-PaNEC, glioblastoma

408   and choroid plexus cancer models we report here are competitive with or outperform the existing

409   *Rb1/Tp53*-inactivated mice models in terms of latency and penetrance of tumor development (Table S4).

410   In synopsis, we demonstrate the use of tissue-restricted multiplexed inactivation in *Xenopus* embryos

411   to functionally identify novel tumor suppressor combinations *in vivo*. This nicely complements AAV-

412   mediated *in vivo* murine CRISPR screens [14,45]. We established novel highly penetrant and short latency

413   genetic *X. tropicalis* cancer models upon multiplex *in vivo* CRISPR/Cas9-mediated inactivation of the *rb1,*

414   *rbl1* and *tp53* tumor suppressor genes. These models will generate novel opportunities for gene function

415   interrogation, therapeutic target identification and pre-clinical drug studies. Finally, showcasing the

416   possibilities of multiplexed CRISPR/Cas9 in delineating novel driver mutations in cancer, we establish

417   formal proof of *rbl1* as a tumor suppressor in glioblastoma and small-cell pancreatic neuroendocrine

418   carcinoma.

419

Material and Methods

Generation of *X.tropicalis* mosaic mutants by CRISPR/Cas9

422   All gRNAs were designed with the CRISPRScan algorithm (http://www.crisprscan.org/) [68]. In this study

423   following sequences were targeted. *Rb1* 5'-GCTGTATGATTGTGCTGTACCGG-3', *rbl1*

424   TGGGCTTGCGCGCTGATGTGGGG,   *tp53*[cr1]   5'-CCTCAACTGAGGATTACGCAGGG-3',   *tp53*[cr2]   5'-

425   GAAGAGCTTGTTGAGGTCGGTGG-3',   *pten*[cr1]   5'-GCGCTTGGGACCTGCTGTTGAGG-3',   *pten*[cr2]   5'-

426   GAGTTACAATTCCCAGCCAAAGG-3'. gRNAs were generated by *in vitro* transcription, employing the oligos

427   shown in supplementary table 5A, and quality control and quantification was performed as described

428   before [69,70]. Recombinant NLS-Cas9-NLS protein was generated as previously described [14]. Natural *X.*

429   *tropicalis* matings were performed and embryos were microinjected in either the two- or the eight-cell

430   stage with injection mixes containing precomplexed gRNA and Cas9 protein as shown in supplementary

431   table 5B. Approval was obtained from the Ethical Committee for Animal Experimentation, Ghent

432   University, Faculty of Science and VIB-Site Ghent (EC2018-079). All methods were carried out in

433   accordance with the relevant guidelines set out by this committee.

434   **Next-generation amplicon sequencing**

435   Targeted amplicon sequencing followed by BATCH-GE analysis was performed for quantitative

436   assessment of genome editing, with the primer pairs shown in supplementary table 5C, as described

437   before [71–73]. For *tp53* genotyping of animals after necropsy, spinal cord (ectoderm targeted) or heart

438   (anterior endoderm targeted) tissue were lysed overnight in lysis buffer (50 mM Tris pH 8.8, 1 mM EDTA,

439   0.5% Tween-20, 200 µg/ml proteinase K) and targeted amplicon sequencing of *tp53* was performed

440   identically as above. For next-generation amplicon sequencing from laser-capture microdissected

441   tumors, PCR input DNA was generated as previously described [69]. PCR amplification relevant genomic

442   regions was performed with the (nested) primers shown in table 5D. All quantitative genome editing

443   efficiencies and INDEL variants, with their relative frequencies, in this study are shown in supplementary

444   Table 1.

445   **Ex-vivo micro-CT imaging**

446   For ex-vivo micro-CT imaging of *tp53* heterozygous animals, cone-beam micro-CT was employed

447   (Triumph-II, TriFoil Imaging, Northridge, CA, USA). A high-resolution micro-CT imaging protocol was used

448   with the following acquisition parameters: one bed position (90 mm field of view), circular trajectory

449   with continuous rotation over 360 degrees, 50 µm focal spot size, 50 µm detector pixel size, 1.3 times

450   magnification, 512 projections, 370 µA tube current and 50 kVp tube voltage, resulting in a total

451   acquisition time of 14 minutes. The acquired projection data were reconstructed into a three-

452   dimensional image with 512x512x1024 matrix and 100 µm voxel size using the Feldkamp-Davis-Kress

453   algorithm.

15

Flow Cytometry and Natt-Herrick leukocyte counting

454

455 Peripheral blood was collected from wild-type or mutant *X. tropicalis* by toe clipping and immediately

456 suspended in cold 0.66x PBS (amphibian PBS or APBS). Cells were fixed for 20 minutes using fresh 2%

457 paraformaldehyde, blocked/permeabilized in 2% Natural Goat Serum, 1% BSA (VWR) and 0.1% Tween 20

458 (Sigma-Aldrich) in APBS solution. After 10 minutes of blocking and permeabilization, cells were incubated

459 for one hour either with a 1:5 dilution of Rat anti Human CD3:Alexa Fluor®647 (0.05 mg/mL) (clone CD3-

460 12; Bio-Rad) or with undiluted CD8 (AM22) mouse hybridoma supernatant (0.05 mg/mL). Cells incubated

461 with hybridoma supernatant were additionally incubated with DyLight® 488 secondary antibody for one

462 hour. Finally, cells were acquired on a 5 laser-BD LSR Fortessa flow cytometer (BD Biosciences) and

463 analyzed using the FlowJo software (Tree Star). For validation, blood was collected by cardiac bleed from

464 euthanized animals and diluted 1:50 in Natt-Herrick (NH) staining solution, prepared as described before

465 [74]. NH preperates were loaded in a Buerker hemocytometer (Marienfeld) where after leukocytes and red

466 blood cells (RBC) were counted. For each data-point in the statistical analysis, leukocytes and RBC were

467 counted in twelve 0.04 mm² regions. Percentage leukocytes was calculated as

468 (#leukocytes/(#leukocytes+#RBC)).

Histology, immunohistochemistry and nuclear modeling of glioblastoma cells

469

470 All macroscopic pictures were taken with a Carl Zeiss StereoLUMAR.V12 stereomicroscope. For

471 quantification of SC-PaNEC sizes, ImageJ was used. For histology, tissues were fixed overnight in 4%

472 paraformaldehyde (PFA) at 4°C. Bone-containing tissues (*e.g.* cranial structures) were decalcified by

473 Morse's solution (10% sodium citrate and 22.5% formic acid) for 6 hours at room temperature. All tissue

474 samples were dehydrated, imbedded in paraffin and 5 µM tissue sections were made by microtomy. For

475 classical histopathology, slides were stained with hematoxylin and eosin. Choroid plexuses were

476 analyzed by a clinical pathologist (D. C.) and assigned a WHO grade. Immunohistochemistry was

477 performed as previously described with primary antibodies: anti-PCNA antibody (PC10; Dako), anti-pHH3

478 antibody (IHC-00061; Bethyl laboratories), anti-CD3 antibody (clone CD3-12; Bio-Rad), anti-GFAP (Z0334;

479 DAKO), anti-cleaved-caspase3 (9661; CST) and anti-EZH2 antibody (A304-197A-T; Bethyl Laboratories) [75].

480 TUNEL was performed using the In Situ Cell Death Detection Kit, AP (11684809910, Roche) according to

481 manufacturer's instructions. In all immunohistochemical experiments, omission of either the primary

482 antibody or the TUNEL labeling mix served as a negative control. For immunofluorescent (IF) goat anti-

483 mouse DyLight-633 (ThermoFisher) and goat anti-rabbit DyLight-633 (ThermoFisher) was used. All IF and

484 TUNEL samples where counterstained with Hoechst-33342. SC-PaNEC PCNA IF was captured with a Leica

485 TCS LSI zoom confocal microscope. Choroid plexus tumor PCNA IF and Hoechst-33324 for glioma nuclear

486 modeling were collected on an LSM880 Airyscan (Carl Zeiss, Jena, Germany) using either a LD LCI Plan-

487 Apochromat 25x/0.8 Imm Korr DIC M27 or a 63x PlanApo NA:1.4 oil immersion DIC M27 objective. The

488 operating software was ZEN blue 2.3. The Airyscan detector was used in both the fast and full

489 superresolution mode. A pixel reassignment algorithm in combination with a Wiener filter were carried

490 out post acquisition. In order to gain nuclear 3D information, z-stacks were recorded and a 3D

491 reconstruction of relevant z-stacks was made in Volocity 6.3.0 (Perking Elmer). Furthermore, nuclear

492 material from glioblastoma cells was segmented, employing MIB, and a 3D model of the nuclear

493 membrane was build using Imaris (Bitplane) [76]. TUNEL, pHH3 and GFAP IF was captured on a Leica TCS

494 SP5 confocal microscope using the tile scan and image stitching function. For IHC with DAB detection of

495 EZH2, PCNA, CD3 and Cleaved-Caspase 3, Goat Anti-Rabbit IgG (H+L) (VEC.BA-1000; Vector laboratories)

496 was used. Signal was developed using the VECTASTAIN Elite ABC HRP Kit (PK-6100; Vector laboratories)

497 and ImmPACT DAB Peroxidase (SK-4105; Vector laboratories). Samples were counterstained 1 minute

498 with hematoxylin. Imaging of H&E stained and DAB/hematoxylin stained sections was performed with a

499 Zeiss Axio Scan.Z1 equipped with a 20X Plan-Apochromat 0.8 NA dry objective, using a Hitachi HV-

500 F202SCL camera. High-magnification photomicrographs of glioblastoma cells were taken with an Zeiss

501 Axioscope using a 100x oil objective. To quantity cell proliferation in tumors, we performed automated

502 counting of pHH3$^+$ cells using ImageJ, normalizing pHH3$^+$ cells over tumor section volume.

Acknowledgments

515   conclusion, we would also like to acknowledge Marjolein Carron for critical proof-reading of this

516   manuscript.

517   **Author information**

518   **Affiliations**

519   *Department of Biomedical Molecular Biology, Ghent University, Ghent, Belgium*
520   Thomas Naert, Dionysia Dimitrakopoulou, Dieter Tulkens, Suzan Demuynck, Liza Eeckhout, Rivka
521   Noelanders,
522   Kris Vleminckx

523   *Cancer Research Institute Ghent, Ghent, Belgium*
524   Thomas Naert, Dionysia Dimitrakopoulou, Dieter Tulkens, Christian Vanhove, Jo Van Dorpe,
525   David Creytens, Kris Vleminckx

526   *Center for Medical Genetics, Ghent University, Ghent, Belgium*
527   Kris Vleminckx

528   *VIB Center for Inflammation Research, Ghent, Belgium*
529   Gert Van Isterdael

530   *Laboratory for Pharmaceutical Biotechnology, Ghent University, B-9000 Ghent, Belgium.*
531   Dieter Deforce

532

533   *Department of Pathology, Ghent University and Ghent University Hospital, Ghent, Belgium*
534   David Creytens, Jo Van Dorpe

535   *Infinity lab, Ghent University Hospital, Ghent, Belgium.*
536   Christian Vanhove

537

538   **Contributions**

539   T.N, D.Di. and K.V. designed the study. D.Di., T.N, D.T. and R.N. were involved in generation and

540   phenotyping of the *tp53* mutant *X. tropicalis*. T.N. performed genome engineering and phenotyping of all

541   *retinoblastoma* and *retinoblastoma/tp53* mutants. T.N., L.E. and D.De were involved in laser-capture

542   microdissection and downstream analysis. D.C. and J.v.D performed pathological analysis. D.T., D.Di. and

543   G.v.I performed flow cytometry experiments. T.N. performed cancer genomic database mining. C.V.

544   performed X-ray imaging. S.D. provided technical assistance throughout the project. T.N. and K.V. wrote

545   the manuscript.

546

547 **References**

548 1. Konukiewitz, B. *et al.* Pancreatic neuroendocrine carcinomas reveal a closer relationship to ductal
549   adenocarcinomas than to neuroendocrine tumors G3. *Hum. Pathol.* **77,** 70–79 (2018).

550 2. Glenn, S. T. *et al.* Conditional deletion of p53 and Rb in the renin-expressing compartment of the
551   pancreas leads to a highly penetrant metastatic pancreatic neuroendocrine carcinoma. *Oncogene*
552   **33,** 5706–15 (2014).

553 3. Tong, Y. *et al.* Cross-Species Genomics Identifies TAF12, NFYC, and RAD54L as Choroid Plexus
554   Carcinoma Oncogenes. *Cancer Cell* **27,** 712–727 (2015).

555 4. McLendon, R. *et al.* Comprehensive genomic characterization defines human glioblastoma genes
556   and core pathways. *Nature* **455,** 1061–1068 (2008).

557 5. Chow, L. M. L. *et al.* Cooperativity within and among Pten, p53, and Rb pathways induces high-
558   grade astrocytoma in adult brain. *Cancer Cell* **19,** 305–16 (2011).

559 6. George, J. *et al.* Comprehensive genomic profiles of small cell lung cancer. *Nature* **524,** 47–53
560   (2015).

561 7. Hann, C. L. & Rudin, C. M. Management of small-cell lung cancer: incremental changes but hope
562   for the future. *Oncology (Williston Park).* **22,** 1486–92 (2008).

563 8. Basturk, O. *et al.* The High-grade (WHO G3) Pancreatic Neuroendocrine Tumor Category Is
564   Morphologically and Biologically Heterogenous and Includes Both Well Differentiated and Poorly
565   Differentiated Neoplasms. *Am. J. Surg. Pathol.* **39,** 683–690 (2015).

566 9. Tabori, U. *et al.* TP53 alterations determine clinical subgroups and survival of patients with
567   choroid plexus tumors. *J. Clin. Oncol.* **28,** 1995–2001 (2010).

568 10. Chow, R. D. *et al.* AAV-mediated direct in vivo CRISPR screen identifies functional suppressors in
569   glioblastoma. *Nat. Neurosci.* **20,** 1329–1341 (2017).

570 11. Dannenberg, J.-H., Schuijff, L., Dekker, M., Van Der Valk, M. & Te Riele, H. Tissue-specific tumor
571   suppressor activity of retinoblastoma gene homologs p107 and p130. (2004).
572   doi:10.1101/gad.322004

573 12. Costa, C., Paramio, J. M. & Santos, M. Skin Tumors Rb(eing) Uncovered. *Front. Oncol.* **3,** 307
574   (2013).

575 13. Robanus-Maandag, E. *et al.* p107 is a suppressor of retinoblastoma development in pRb-deficient
576   mice. *Genes Dev.* **12,** 1599–609 (1998).

577 14. Naert, T. *et al.* CRISPR/Cas9 mediated knockout of rb1 and rbl1 leads to rapid and penetrant
578   retinoblastoma development in Xenopus tropicalis. *Sci. Rep.* **6,** (2016).

579 15. MacPherson, D. *et al.* Murine bilateral retinoblastoma exhibiting rapid-onset, metastatic
580   progression and N-myc gene amplification. *EMBO J.* **26,** 784–94 (2007).

581 16. Xiao, A., Wu, H., Pandolfi, P. P., Louis, D. N. & Van Dyke, T. Astrocyte inactivation of the pRb

582   pathway predisposes mice to malignant astrocytoma development that is accelerated by PTEN
583   mutation. *Cancer Cell* **1,** 157–68 (2002).

584 17.   Lu, X. *et al.* Selective Inactivation of p53 Facilitates Mouse Epithelial Tumor Progression without
585   Chromosomal Instability. *Mol. Cell. Biol.* **21,** 6017–6030 (2001).

586 18.   Naert, T., Van Nieuwenhuysen, T. & Vleminckx, K. TALENs and CRISPR/Cas9 fuel genetically
587   engineered clinically relevant *Xenopus tropicalis* tumor models. *genesis* **55,** e23005 (2017).

588 19.   DeLay, B. D. *et al.* Tissue-specific Gene Inactivation in *Xenopus laevis* : Knockout of *lhx1* in the
589   Kidney with CRISPR/Cas9. *Genetics* genetics.300468.2017 (2017).
590   doi:10.1534/genetics.117.300468

591 20.   Wirt, S. E. & Sage, J. p107 in the public eye: an Rb understudy and more. *Cell Div.* **5,** 9 (2010).

592 21.   Li, F. P. & Fraumeni, J. F. Soft-tissue sarcomas, breast cancer, and other neoplasms. A familial
593   syndrome? *Ann. Intern. Med.* **71,** 747–52 (1969).

594 22.   Malkin, D. *et al.* Germ line p53 mutations in a familial syndrome of breast cancer, sarcomas, and
595   other neoplasms. *Science* **250,** 1233–8 (1990).

596 23.   Bougeard, G. *et al.* Revisiting Li-Fraumeni Syndrome From *TP53* Mutation Carriers. *J. Clin. Oncol.*
597   **33,** 2345–2352 (2015).

598 24.   Donehower, L. A. *et al.* Mice deficient for p53 are developmentally normal but susceptible to
599   spontaneous tumours. *Nature* **356,** 215–221 (1992).

600 25.   Jacks, T. *et al.* Tumor spectrum analysis in p53-mutant mice. *Curr. Biol.* **4,** 1–7 (1994).

601 26.   Purdie, C. A. *et al.* Tumour incidence, spectrum and ploidy in mice with a large deletion in the p53
602   gene. *Oncogene* **9,** 603–9 (1994).

603 27.   Ignatius, M. S. *et al.* tp53 deficiency causes a wide tumor spectrum and increases embryonal
604   rhabdomyosarcoma metastasis in zebrafish. *Elife* **7,** (2018).

605 28.   Berghmans, S. *et al.* tp53 mutant zebrafish develop malignant peripheral nerve sheath tumors.
606   *Proc. Natl. Acad. Sci.* **102,** 407–412 (2005).

607 29.   Manning, A. L., Benes, C. & Dyson, N. J. Whole chromosome instability resulting from the
608   synergistic effects of pRB and p53 inactivation. *Oncogene* **33,** 2487–94 (2014).

609 30.   Levine, A. J. p53, the Cellular Gatekeeper for Growth and Division. *Cell* **88,** 323–331 (1997).

610 31.   Eischen, C. M. Genome Stability Requires p53. *Cold Spring Harb. Perspect. Med.* **6,** a026096
611   (2016).

612 32.   Naert, T. & Vleminckx, K. CRISPR/Cas9 disease models in zebrafish and Xenopus: The genetic
613   renaissance of fish and frogs. *Drug Discov. Today Technol.* **28,** 41–52 (2018).

614 33.   Lau, C.-H. & Suh, Y. In vivo genome editing in animals using AAV-CRISPR system: applications to
615   translational research of human disease. *F1000Research* **6,** 2153 (2017).

616 34.   Boel, A. *et al.* BATCH-GE: Batch analysis of Next-Generation Sequencing data for genome editing

617   assessment. *Sci. Rep.* **6,** 30330 (2016).

618   35.   Neely, H. R., Guo, J., Flowers, E. M., Criscitiello, M. F. & Flajnik, M. F. 'Double-duty' conventional
619   dendritic cells in the amphibian *Xenopus* as the prototype for antigen presentation to B cells. *Eur.*
620   *J. Immunol.* **48,** 430–440 (2018).

621   36.   Ward, J. M. *et al.* Splenic marginal zone B-cell and thymic T-cell lymphomas in p53-deficient mice.
622   *Lab. Invest.* **79,** 3–14 (1999).

623   37.   Wang, Z. *et al.* Pseudo-hemorrhagic region formation in pancreatic neuroendocrine tumors is a
624   result of blood vessel dilation followed by endothelial cell detachment. *Oncol. Lett.* **15,** 4255–
625   4261 (2018).

626   38.   Montoliu, L. Mendel: a simple excel workbook to compare the observed and expected
627   distributions of genotypes/phenotypes in transgenic and knockout mouse crosses involving up to
628   three unlinked loci by means of a χ2 test. *Transgenic Res.* **21,** 677–681 (2012).

629   39.   Chiou, S.-H. *et al.* Pancreatic cancer modeling using retrograde viral vector delivery and in vivo
630   CRISPR/Cas9-mediated somatic genome editing. *Genes Dev.* **29,** 1576–85 (2015).

631   40.   Maresch, R. *et al.* Multiplexed pancreatic genome engineering and cancer induction by
632   transfection-based CRISPR/Cas9 delivery in mice. *Nat. Commun.* **7,** (2016).

633   41.   van Zoest, I. D., Heijmen, P. S., Cruijsen, P. M. J. M. & Jenks, B. G. Dynamics of background
634   adaptation in Xenopus laevis: Role of catecholamines and melanophore-stimulating hormone.
635   *Gen. Comp. Endocrinol.* **76,** 19–28 (1989).

636   42.   Marino, S., Vooijs, M., van Der Gulden, H., Jonkers, J. & Berns, A. Induction of medulloblastomas
637   in p53-null mutant mice by somatic inactivation of Rb in the external granular layer cells of the
638   cerebellum. *Genes Dev.* **14,** 994–1004 (2000).

639   43.   McEvoy, J. *et al.* Coexpression of normally incompatible developmental pathways in
640   retinoblastoma genesis. *Cancer Cell* **20,** 260–75 (2011).

641   44.   Louis, D. N. *et al.* The 2016 World Health Organization Classification of Tumors of the Central
642   Nervous System: a summary. *Acta Neuropathol.* **131,** 803–820 (2016).

643   45.   Chow, R. D. *et al.* AAV-mediated direct in vivo CRISPR screen identifies functional suppressors in
644   glioblastoma. *Nat. Neurosci.* **20,** 1329–1341 (2017).

645   46.   Jin, X. *et al.* Targeting glioma stem cells through combined BMI1 and EZH2 inhibition. *Nat. Med.*
646   **23,** 1352–1361 (2017).

647   47.   Steed, T. C. *et al.* Differential localization of glioblastoma subtype: implications on glioblastoma
648   pathogenesis. *Oncotarget* **7,** 24899–24907 (2016).

649   48.   Koul, D. PTEN signaling pathways in glioblastoma. *Cancer Biol. Ther.* **7,** 1321–5 (2008).

650   49.   Schaffer, B. E. *et al.* Loss of p130 accelerates tumor development in a mouse model for human
651   small-cell lung carcinoma. *Cancer Res.* **70,** 3877–83 (2010).

652   50.   Yachida, S. *et al.* Small Cell and Large Cell Neuroendocrine Carcinomas of the Pancreas are

653   Genetically Similar and Distinct From Well-differentiated Pancreatic Neuroendocrine Tumors. *Am.*
654   *J. Surg. Pathol.* **36,** 173–184 (2012).

655 51. Abou-El-Ardat, K. *et al.* Comprehensive molecular characterization of multifocal glioblastoma
656   proves its monoclonal origin and reveals novel insights into clonal evolution and heterogeneity of
657   glioblastomas. *Neuro. Oncol.* **19,** 546–557 (2017).

658 52. Wiedemeyer, W. R. *et al.* Pattern of retinoblastoma pathway inactivation dictates response to
659   CDK4/6 inhibition in GBM. *Proc. Natl. Acad. Sci. U. S. A.* **107,** 11501–6 (2010).

660 53. Cerami, E. *et al.* The cBio Cancer Genomics Portal: An Open Platform for Exploring
661   Multidimensional Cancer Genomics Data. *Cancer Discov.* **2,** 401–404 (2012).

662 54. Gao, J. *et al.* Integrative Analysis of Complex Cancer Genomics and Clinical Profiles Using the
663   cBioPortal. *Sci. Signal.* **6,** pl1-pl1 (2013).

664 55. Liu, F. *et al.* MicroRNA-106b-5p boosts glioma tumorigensis by targeting multiple tumor
665   suppressor genes. *Oncogene* **33,** 4813–4822 (2014).

666 56. Vitucci, M. *et al.* Genomic profiles of low-grade murine gliomas evolve during progression to
667   glioblastoma. *Neuro. Oncol.* **19,** 1237–1247 (2017).

668 57. Wojton, J. *et al.* Systemic Delivery of SapC-DOPS Has Antiangiogenic and Antitumor Effects
669   Against Glioblastoma. *Mol. Ther.* **21,** 1517–1525 (2013).

670 58. Vanderluit, J. L. *et al.* p107 regulates neural precursor cells in the mammalian brain. *J. Cell Biol.*
671   **166,** 853–863 (2004).

672 59. Vanderluit, J. L. *et al.* The Retinoblastoma family member p107 regulates the rate of progenitor
673   commitment to a neuronal fate. *J. Cell Biol.* **178,** 129–139 (2007).

674 60. Harb, G., Vasavada, R. C., Cobrinik, D. & Stewart, A. F. The retinoblastoma protein and its
675   homolog p130 regulate the G1/S transition in pancreatic beta-cells. *Diabetes* **58,** 1852–62 (2009).

676 61. Cai, E. P. *et al.* Rb and p107 are required for alpha cell survival, beta cell cycle control and
677   glucagon-like peptide-1 action. *Diabetologia* **57,** 2555–2565 (2014).

678 62. Vasavada, R. C., Cozar-Castellano, I., Sipula, D. & Stewart, A. F. Tissue-specific deletion of the
679   retinoblastoma protein in the pancreatic beta-cell has limited effects on beta-cell replication,
680   mass, and function. *Diabetes* **56,** 57–64 (2007).

681 63. Konukiewitz, B. *et al.* Somatostatin receptor expression related to TP53 and RB1 alterations in
682   pancreatic and extrapancreatic neuroendocrine neoplasms with a Ki67-index above 20%. *Mod.*
683   *Pathol.* **30,** 587–598 (2017).

684 64. Konukiewitz, B. *et al.* Pancreatic neuroendocrine carcinomas reveal a closer relationship to ductal
685   adenocarcinomas than to neuroendocrine tumors G3. *Hum. Pathol.* **77,** 70–79 (2018).

686 65. Merino, D. M. *et al.* Molecular Characterization of Choroid Plexus Tumors Reveals Novel Clinically
687   Relevant Subgroups. *Clin. Cancer Res.* **21,** 184–192 (2015).

688 66. Solin, S. L., Shive, H. R., Woolard, K. D., Essner, J. J. & McGrail, M. Rapid tumor induction in

689   zebrafish by TALEN-mediated somatic inactivation of the retinoblastoma1 tumor suppressor rb1.
690   *Sci. Rep.* **5,** 13745 (2015).

691   67.   Shim, J. *et al.* Development of zebrafish medulloblastoma-like PNET model by TALEN-mediated
692   somatic gene inactivation. *Oncotarget* **8,** 55280–55297 (2017).

693   68.   Moreno-Mateos, M. A. *et al.* CRISPRscan: designing highly efficient sgRNAs for CRISPR-Cas9
694   targeting in vivo. *Nat. Methods* **12,** 982–8 (2015).

695   69.   Naert, T. & Vleminckx, K. *CRISPR/cas9-mediated knockout of RB1 in xenopus tropicalis*. *Methods in*
696   *Molecular Biology* **1726,** (2018).

697   70.   Naert, T. & Vleminckx, K. Methods for CRISPR/Cas9 Xenopus tropicalis Tissue-Specific Multiplex
698   Genome Engineering. *Methods Mol. Biol.* **1865,** 33–54 (2018).

699   71.   Steyaert, W., Boel, A., Coucke, P. & Willaert, A. BATCH-GE: Analysis of NGS Data for Genome
700   Editing Assessment. *Methods Mol. Biol.* **1865,** 83–90 (2018).

701   72.   Naert, T. & Vleminckx, K. Genotyping of CRISPR/Cas9 Genome Edited Xenopus tropicalis. *Methods*
702   *Mol. Biol.* **1865,** 67–82 (2018).

703   73.   Szenker-Ravi, E. *et al.* RSPO2 inhibition of RNF43 and ZNRF3 governs limb development
704   independently of LGR4/5/6. *Nature* **557,** 564–569 (2018).

705   74.   Maxham, L. A., Forzán, M. J., Hogan, N. S., Vanderstichel, R. V. & Gilroy, C. V. Hematologic
706   reference intervals for *Xenopus tropicalis* with partial use of automatic counting methods and
707   reliability of long-term stored samples. *Vet. Clin. Pathol.* **45,** 291–299 (2016).

708   75.   Naert, T. & Vleminckx, K. Cancer Models in Xenopus tropicalis by CRISPR/Cas9 Mediated Knockout
709   of Tumor Suppressors. *Methods Mol. Biol.* **1865,** 147–161 (2018).

710   76.   Belevich, I., Joensuu, M., Kumar, D., Vihinen, H. & Jokitalo, E. Microscopy Image Browser: A
711   Platform for Segmentation and Analysis of Multidimensional Datasets. *PLOS Biol.* **14,** e1002340
712   (2016).

713

714

715

716

717   **Figure Legends**

718   **Figure 1. *Tp53* mutant *X. tropicalis* develop hematological malignancy and sarcomas. (A)** Kaplan-Meier

719   survival analysis on cohorts consisting of two clutches of *tp53* homozygous knockout (n=6; red and n=7;

720   blue) and one clutch of heterozygous *tp53* knockout (n=14; black) *X. tropicalis*. Statistical analysis was

721   done using the Prism Mantel-Cox test (ns – not significant; ** $p < 0.01$; *** $p < 0.001$). Chi-Squared

722   values and the Hazard ratios are listed in Supplementary table 2A. **(B)** X-ray imaging of a 28-month old

723   *tp53*$^{+/\Delta4var2}$ demonstrating ectopic calcified structures (white arrows). **(C)** (Left panels) In the wild-type

724   spleen, CD3$^+$ T-cells form a ring-like structure around the PCNA$^+$ B-cells located in the white pulp. (Right

725   panels) Disruption of a normal CD3$^+$ ring-like structure observed in a *tp53*$^{\Delta4var2/\Delta4var2}$ animal is indicative

726   of hematological malignancy. **(D)** Pie chart summarizing the observed splenic immunostaining for CD3

727   and PCNA in *tp53*$^{\Delta4var1/\Delta4var2}$ animals. Staining patterns being either normal or with loss of the typical CD3$^+$

728   ring structure with or without ectopic staining of PCNA in the red pulp. **(E)** Photomicrograph of Natt-

729   Herrick stained blood demonstrating a cluster of leukocytes and a normal nucleated erythrocyte. Inset

730   demonstrates a high magnification photomicrograph of a lymphoblast. **(F)** Flow cytometry analysis

731   reveals an increased number of both CD3$^+$ (left) and CD8$^+$ lymphoblasts (right) in peripheral blood of a

732   *tp53*$^{\Delta4var1/\Delta4var2}$ animal, when compared to an age-matched control. **(G)** Histopathology of the liver reveals

733   diffuse infiltration of T-lymphoblasts, also enriched within liver capillary (white arrow; top inset) and in

734   between the liver parenchymal cells (black arrow). **(H)** Sarcoma in a *tp53*$^{+/\Delta4var2}$ animal observed upon

735   gross examination, with associated histopathology and demonstration of malignant nature by PCNA

736   proliferation staining. White scale bar is 100 µm and black scale bar is 5 µM.

737   **Figure 2. Small-cell pancreatic neuroendocrine carcinoma (SC-PaNEC) in *X. tropicalis* upon mosaic**

738   **CRISPR/Cas9 genome editing of *rb1* and *rbl1* in the anterior endoderm. (A)** Breeding and CRISPR/Cas9

739   injection scheme demonstrating the generation of the single mutant KO (smKO -orange) (*rb1*

740   CRISPR/Cas9 injection in embryos obtained from a *tp53*$^{\Delta4var1/+}$ x *tp53*$^{\Delta4var2/+}$ intercross), double mutant KO

741   (dmKO - blue) (*rb1/rbl1* CRISPR/Cas9 injection in embryos obtained from a *tp53*$^{\Delta4var1/+}$ x *tp53*$^{\Delta4var2/+}$

742   intercross) and triple mutant KO (tmKO - purple) (*rb1/rbl1/tp53* CRISPR/Cas9 injection in embryos

743   obtained from intercrossing WT animals). **(B)** Typical external pathology of a pancreatic tumor occurring

744   in a tmKO animal. The inset shows an age-matched control pancreas. **(C)** Tumor incidence curves and

745   Kaplan-Meier analysis comparing smKO (n=13), dmKO (n=29) and tmKO (n=22) genotypes. Statistical

746   analysis, done using the Prism Mantel-Cox test, revealed that SC-PaNEC incidences were significantly

747   different across the experimental setups ($p < 0.0001$). Chi-Squared values and the Hazard ratios are listed

24

748   in supplementary table 2C. **(D)** H&E stain of pancreatic tumors shows recurrent histological features of

749   SC-PaNEC with necrotic foci (nec). The black arrow indicates non-neoplastic pancreatic tissue. The inset

750   shows, under higher magnification, diffuse sheets of poorly differentiated cells with small blue round

751   morphology, nuclear pleomorphism and hemorrhages (yellow arrows). **(E)** SC-PaNEC sections

752   immunostained for pHH3 or PCNA, counterstained with Hoechst-33342, reveal high proliferative

753   capacity. **(F)** Laser-capture microdissection (LCM) of dmKO SC-PaNEC reveals chromosomal instability in

754   $tp53^{-/-}$ tumors. In $tp53^{+/del4}$ tumors the allelic ratio of the mutant allele remains around 50% (right graph).

755   In contrast, two out of three $tp53^{-/-}$ tumors show substantial deviation from the expected allelic ratios

756   (50% each variant) (left graph). **(G)** Percentage of mutant *rbl1* and *tp53* reads observed in LCM-derived

757   SC-PaNECs sampled from either tmKO (left) or dmKO (right) animals. Red bullets and blue bullets

758   demarcate SC-PaNECs with monoallelic inactivating *tp53* mutations in the tmKO and dmKO setup,

759   respectively. White scale bar is 500μm, black scale bar is 50μm.

760   **Figure 3. *Rb1* and *rbl1* crispants (ectodermal targeted) develop retinoblastoma, excessive black skin**

761   **pigmentation and a spectrum of brain tumors. (A)** CRISPR/Cas9 targeting of *rb1* and *rbl1* in ectodermal

762   lineage via unilateral injection of an animal-dorsal blastomere. **(B)** Unilateral ectodermal targeting of

763   *rb1/rbl1* CRISPR/Cas9, in *tp53* wild-type, heterozygous or compound heterozygous background, results in

764   crispants developing externally visible retinoblastoma (75%; n=16) and excessive skin pigmentation

765   (44%; n=16). Inset shows an animal from the same clutch without external symptoms. **(C)** H&E stained

766   section illustrating increased pigment deposition internal to the stratified epithelium (black arrow). Inset

767   is an animal from the same clutch showing normal pigment deposition. **(D)** H&E stained section of the

768   animal shown in panel A. Unilateral retinoblastoma (black arrow) can clearly be distinguished. Inset

769   shows higher magnification of the retinoblastoma illustrating the classic histopathological characteristics

770   (homer-wright rosettes). **(E)** H&E stained horizontal brain section (anterior side of the animal to the left)

771   revealing multiple neoplasms. Two distinct poorly differentiated, highly malignant, small-blue round cell

772   tumors of unknown origin are shown, most likely representing trilateral retinoblastoma and

773   medulloblastoma (white arrow). Furthermore, a choroid plexus neoplasm can clearly be distinguished

774   within an expanded ventricle (black arrow) and the forebrain harbors a glioblastoma lesion (red arrow).

775   Inset shows the normal *X. tropicalis* brain architecture. White scale bar is 1mm, black scale bar is 100

776   μM.

777   **Figure 4: Choroid plexus (CP) tumors arising in *rb1/rbl1* crispants differ in grade according to their *tp53***

778   **genotype. (A)** H&E stained sections of choroid plexuses representative for the CPT tumor grades

779   observed within the clutch. (Top panels) Normal choroid plexus architecture consists out of a layer of

780   ependymal cells, underlying capillaries and pia mater. Insets demonstrate both gross (left) and

781   histological (right) normal CP architecture. Note that in *Xenopus*, the erythrocytes are nucleated. (Middle

782   panels) WHO grade 1 (G1) CP neoplasm with cellular disarray, (pseudo)-stratification, atypia and loss of

783   polarization (black arrow). (Bottom panels) WHO > G1 CP neoplasm with pronounced atypia and

784   aggressive growth characteristics. **(B)** Choroid plexus tumor in a *tp53*$^{+/-}$ animal showcasing clear

785   continuity between normal CP and neoplastic tissue. **(C)** Association between *tp53* genotype and grade

786   of choroid plexus lesions (*p* < 0.01; Table S2H). **(D)** >G1 CP neoplasm immunostained for PCNA (red),

787   counterstained with Hoechst-33342, reveals high proliferative capacity within highly atypical tumor areas

788   (white arrow). **(E)** Laser-capture microdissection (LCM) of CP tumors (CPT) reveals chromosomal

789   instability, as can be appreciated by the differential *tp53* allelic ratios between control and CPT tissues.

790   Left (*tp53*$^{Δ4/Δ4}$) control bar show the average of LCM control tissues (n = 2). Right (*tp53*$^{Δ4/+}$) control is the

791   allelic ratio in spinal cord control tissue from the animal carrying CPT-5. Gray scale bar is 500 μM, white

792   scale bar is 100 μM, black scale bar is 50μM. White scale bar in panel D is 10 μM.

793   **Figure 5: *Rbl1* functions as a tumor suppressor in glioblastoma, while *tp53* inactivation underlies**

794   **progression. (A)** H&E stained sections of *Xenopus* forebrains containing representative histopathology of

795   low-grade glioma (left-middle) and high-grade glioblastoma (right) occurring across different

796   experimental conditions. **(B)** (Left panel) Low grade glioma with the occasional multinucleated giant cell

797   in *tp53* wild-type and heterozygous animals, targeted in the ectodermal lineage with *rb1* and *rbl1*

798   CRISPR/Cas9. (Right panel) However, when similarly targeting *rb1* and *rbl1* in a *tp53* nullizygous animals,

799   higher-grade glioblastoma lesions develop. **(C)** Quadruple multiplex CRISPR/Cas9-mediated targeting of

800   *rb1*, *rbl1*, *tp53* and *pten* in the ectodermal lineage leads to fully penetrant (100%; n=13) development of

801   high-grade glioblastoma lesions at day 42. **(D)** Bar plot representing absence or presence of either low-

802   grade glioma or high-grade glioblastoma lesions across the performed experimental setups. Genes

803   shown in bold were edited in the ectodermal lineage by CRISPR/Cas9, while *tp53* genotypes, shown in

804   grey, were germline inherited. **(E)** (top) PCNA immunostaining reveals high proliferative index in

805   glioblastoma cells. (bottom) EZH2 immunostaining reveals EZH2 expression in glioblastoma cells, but

806   absence of expression in the subventricular zone (black arrow). Black scale bar is 100 μM and white scale

807   bar is 20 μM.

808   **Supplemental movie 1: Central glioblastoma cell with nuclear aneuploidy and increased number of**

809   **nucleoli, surrounded by normal neurons demonstrating two nucleoli.** 3D-reconstruction of Hoechst-

810   33342 stained nuclei followed by segmented 3D-model of glioblastoma nuclear membrane. This movie

811   demonstrates heavily increased number of nucleoli within the glioblastoma cell.

812   **Supplemental movie 2**: **Massive interconnected nuclear abnormalities in glioblastoma.** 3D-

813   reconstruction of Hoechst-33342 stained nuclei followed by segmented 3D-model of glioblastoma

814   nuclear membrane. This movie demonstrates that nuclear material in seemingly disconnected

815   glioblastoma cells can in fact be interconnected.

816   ## Supplementary data: Tables

817   **Table S1: Genotyping by PCR amplification, sequencing (MiSeq) and BATCH-GE analysis**. Genotyping

818   performed throughout this study after BATCH-GE processing with genome editing efficiencies and

819   variant calls, subdivided in letter-coded sheets.

820   **Table S2: Statistical Analyses**. Raw data and statistical tests performed throughout this study, subdivided

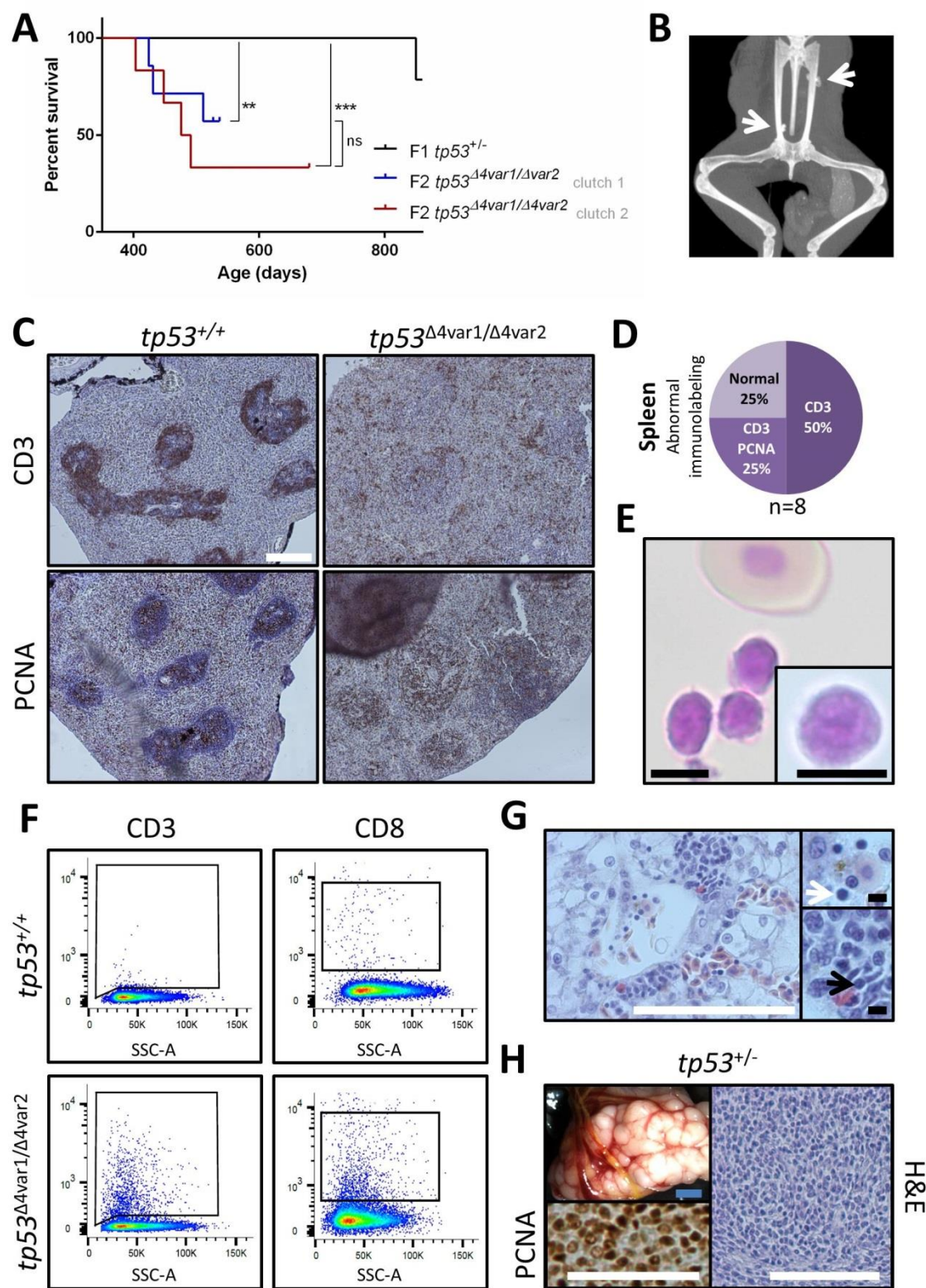821   in letter coded sheets.

822   **Table S3: Analysis of co-occurrence of RB1 and RBL1 alterations in human glioma.**

823   **Table S4: Comparison between established, closest prior art, mice cancer models and the novel**

824   ***Xenopus* models presented in this study in terms of time-to-onset and penetrance of cancer**

825   **phenotypes.**

826   **Table S5: Primer sequences used for PCR amplification, oligo sequences used for gRNA synthesis and**

827   **concentrations of injected CRISPR/Cas9 ribonucleoprotein complexes.**
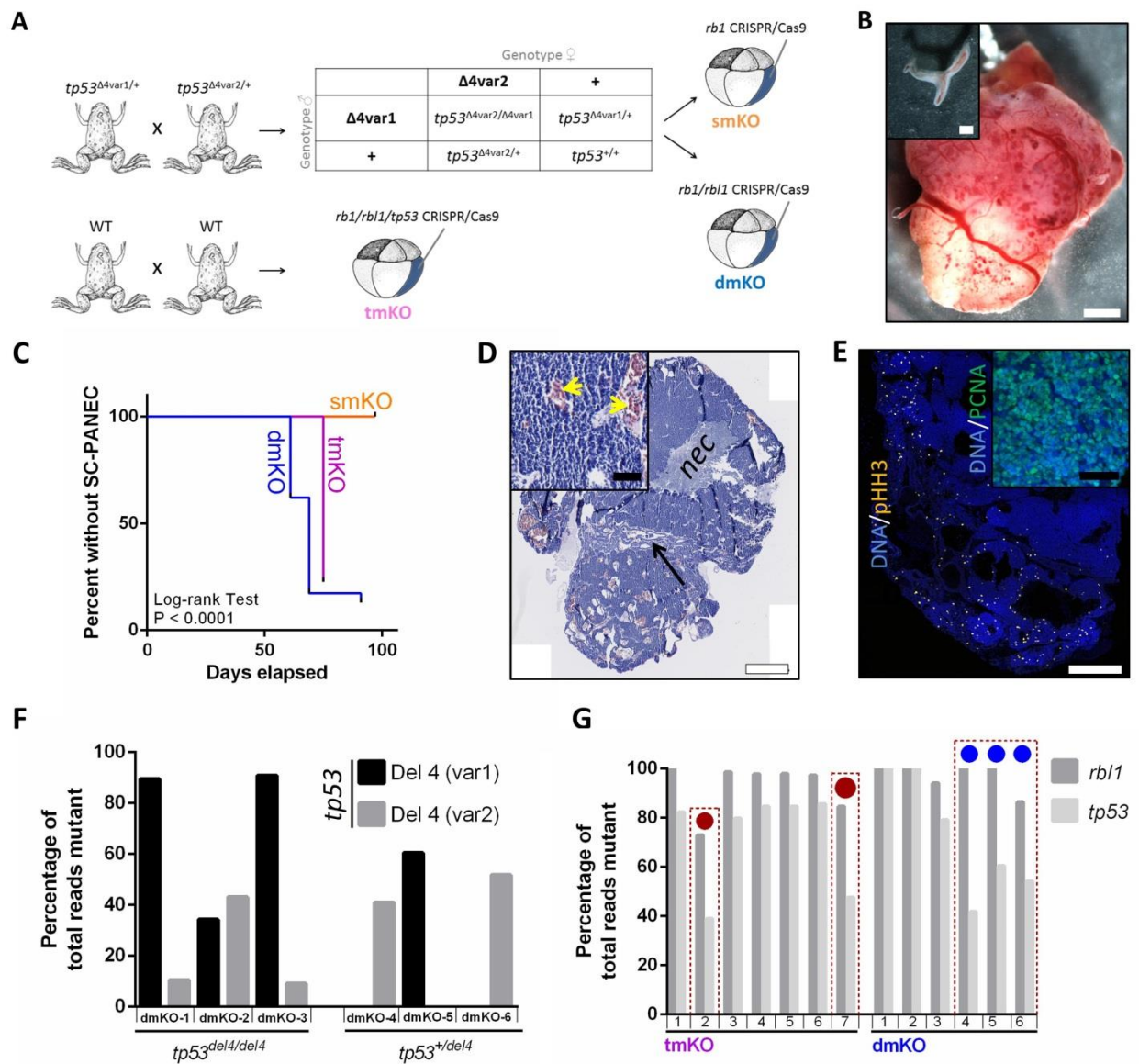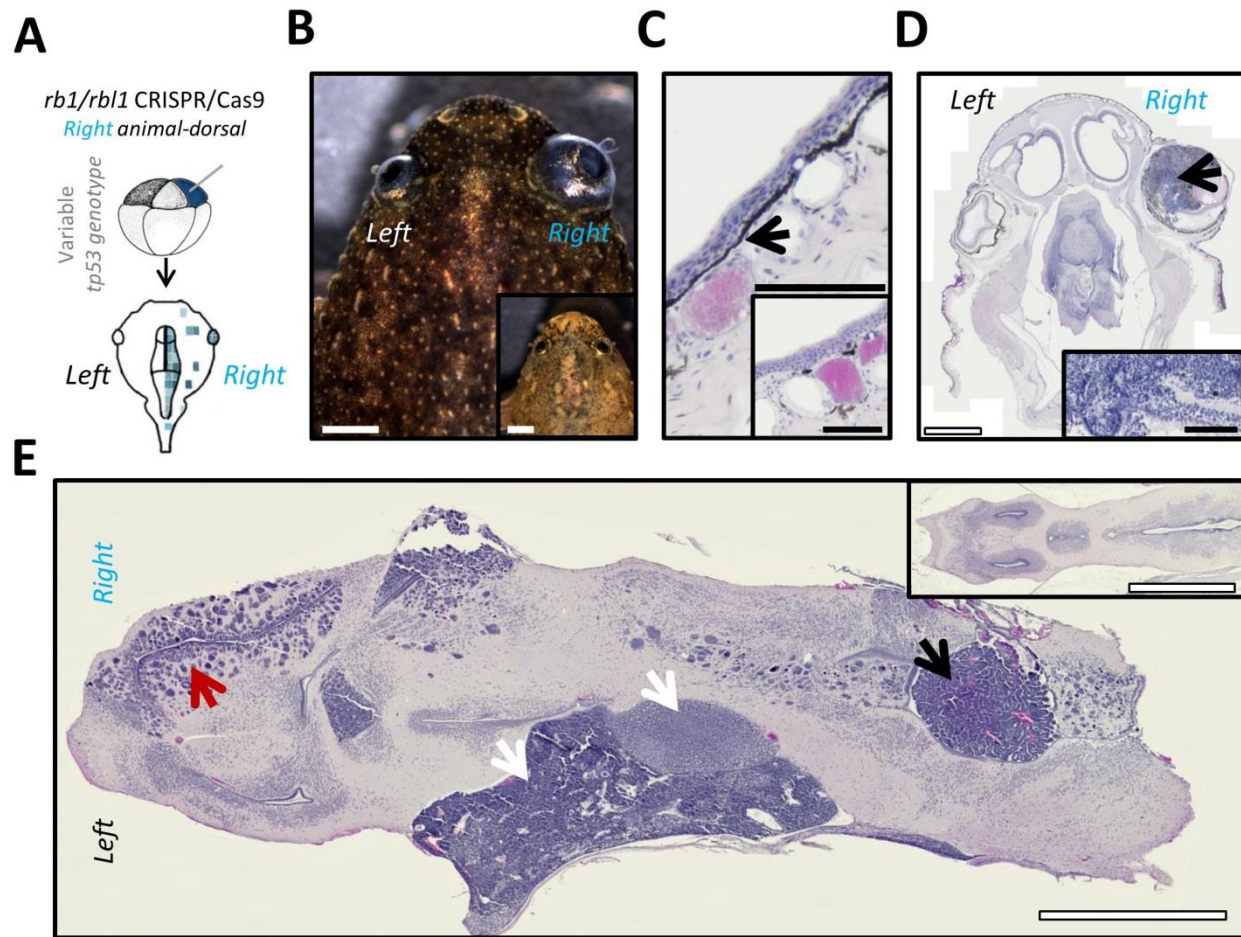
828

829 **Figure 1**
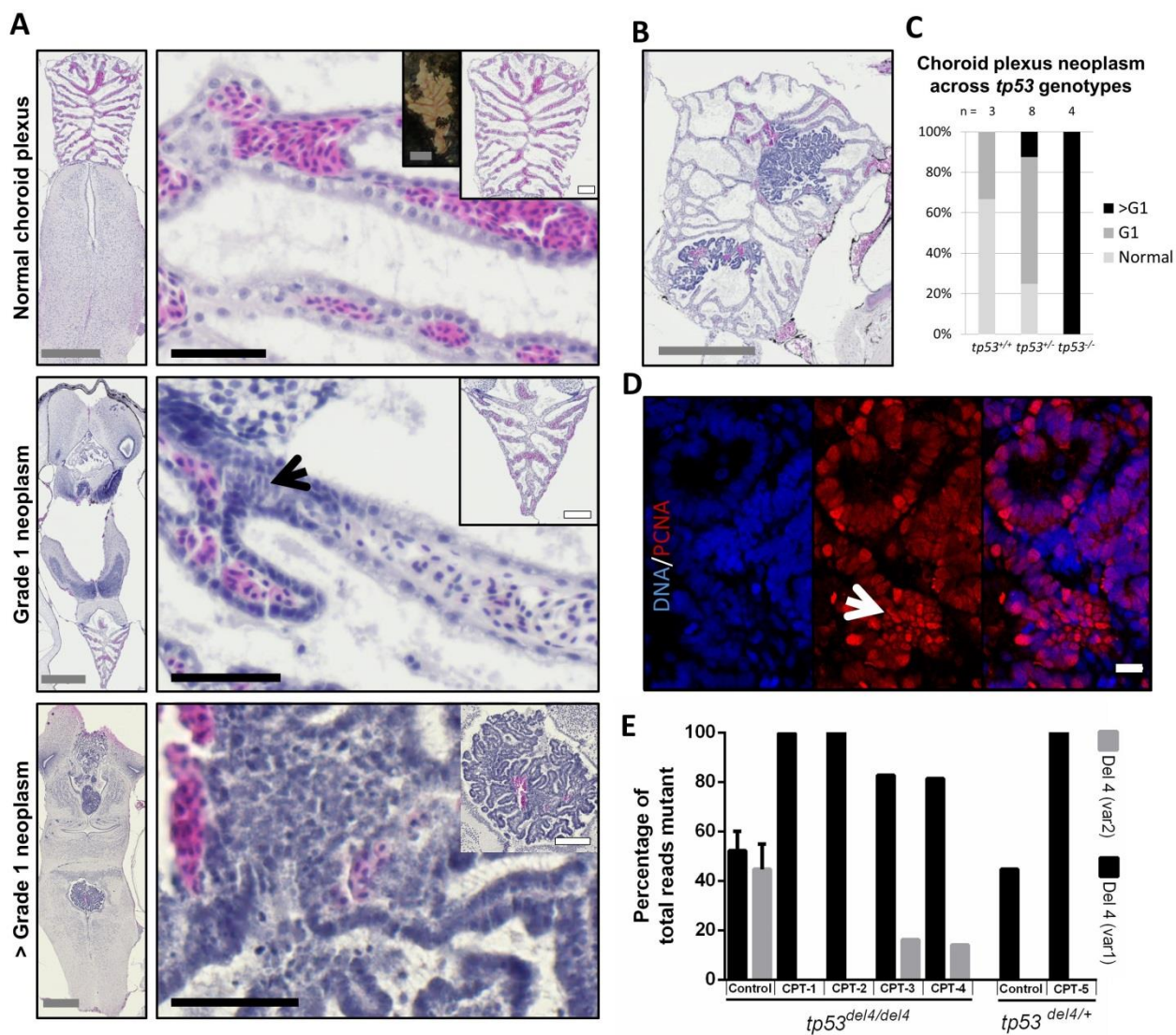
831 **Figure 2**

834   **Figure 3**

835
836

837 **Figure 4**

838
839

840 **Figure 5**

841